One-pot Synthesized, Fe-Incorporated Self-Standing Carbons with a Hierarchical Porosity Remove Carbamazepine and Sulfamethoxazole through Heterogeneous Electro-Fenton

Mojtaba Mohseni[a,b], Wibke Zängler[a], Kristof Demeestere[b], Gijs Du Laing[b], Sabita Bhandari[c], Anna K. Mechler[c], Süleyman Yüce[a], Robert G. Keller[a], Matthias Wessling[a,d,*]

[a] *RWTH Aachen University, Aachener Verfahrenstechnik - Chemical Process Engineering, Forckenbeckstr. 51, 52074 Aachen, Germany*
[b] *Ghent University, Department of Green Chemistry and Technology, Coupure Links 653, 9000 Ghent, Belgium*
[c] *RWTH Aachen University, Aachener Verfahrenstechnik - Electrochemical Reaction Engineering, Forckenbeckstr. 51, 52074 Aachen, Germany*
[d] *DWI - Leibniz Institute for Interactive Materials, Forckenbeckstr. 50, 52074 Aachen, Germany*

Abstract

Hierarchically porous carbons (HPC) are promising electrode materials for heterogeneous electro-Fenton (HEF), where in-situ produced hydrogen peroxide (H_2O_2) on the carbon surface reacts with the adjacently-immobilized catalyst to form unselective radicals. However, the synthesis of HPC usually comprises several steps, particularly catalyst-containing HPC. Moreover, with or without catalysts, most of previously reported HPCs were produced or ultimately used as powders, requiring additional efforts (e.g., adding polymeric binders) to make a functional electrode. Besides blocking some catalyt-

*Corresponding Author: M. Wessling
Email address: manuscripts.cvt@avt.rwth-aachen.de (Matthias Wessling)
[1]Link to the accepted and published version: https://doi.org/10.1016/j.cej.2022.137006

ically active carbon sites and the immobilized catalysts, polymeric binders pose risks of secondary pollution due to their undesired release since they are polyfluorinated compounds. This study introduces a one-pot method to synthesize Fe-incorporated self-standing HPCs with potential scalability. HEF experiments demonstrated the catalysts' activity for the formation of radicals, negligible catalyst leaching at both pH 3 and 7, and good reusability of as-synthesized HPC electrodes while elaborating on different diffusion-controlled degradation mechanisms.

Keywords:
Electrochemical Advanced Oxidation Processes (EAOPs), Freestanding hierarchically Porous Carbons, Heterogeneous Catalysis, Micropollutants Removal, Oxygen Reduction Reactions

---

1. Introduction

Electrochemical advanced oxidation processes (EAOP), where electrochemical generation of highly reactive radicals ($^{\bullet}$OH) occurs, emerge as promising technologies for removing persistent organic micropollutants (OMPs) as they have shown the capability of mineralizing various organic components [1–3]. Advantages of these processes are versatility, high energy efficiency, and mild operational conditions [1, 4]. Moreover, the primary form of energy required for EAOPs is electrical, which can be supplied by renewable energy sources [2]. Anodic oxidation, electro-Fenton (EF), photoelectro-Fenton, and sonoelectrolysis are examples of EAOPs [5]. Among them, EF is an eco-friendly, cost-effective, and powerful treatment technique [2, 4, 6], where electro-generated H_2O_2, via two-electron oxygen re-

duction reaction [7, 8], reacts with ferrous ions (Fe^{2+}) to form $^{\bullet}OH$ [1, 7].

Nonetheless, EF only operates at acidic pH (2.8 - 3.5) because of the insolubility of iron catalysts at higher pH values (pH $>$ 4), which precludes its direct implementation for water/wastewater treatment [6]. Operational acidic pH demands chemicals for acidification and a posterior neutralization of water streams, which, in turn, produces sludge with no possibility for catalyst recycling. On the other hand, catalyst immobilization widens EF's pH window as there are no dissolved catalysts to be precipitated at circumneutral pH values, meaning that no acidification/neutralization is required for water/wastewater treatment [9]. Besides that, fixed catalysts offer the advantage of being recyclable and might be reusable for several runs. Thus, EF with immobilized catalysts, or heterogeneous EF (HEF), can realize EF's direct implementation for degradation of persistent OMPs in water. A HEF process can be performed either with a suspension of solid catalysts, which are separable and recyclable from bulk solution or with catalyst-containing electrodes [6]. In the former case, the produced H_2O_2 on the electrode's surface needs to move toward the bulk solution to meet suspended solid catalysts for further reactions. In the latter one, however, the produced H_2O_2 reacts with adjacently-immobilized catalysts for $^{\bullet}OH$ formation [9], offering less process complexity and minimized mass transport limitations [10, 11]. Hence, developing efficient Fe-containing electrodes for HEF processes has gained lots of attention over the past few years, especially Fe-containing carbons [9, 12–18] given their low production costs and intrinsic features like high specific surface area, large porosity, chemical stability, and thermal and electrical conductivity [6].

Three-dimensional (3D) carbons like activated carbon fiber (ACF) [19], carbon felt (CF) [20, 21] and graphite felt (GF) [22, 23] have been widely used as electrodes for HEF given their freestanding geometry and relatively high surface to volume ratios, which is necessary for module design and process modification [14]. Nevertheless, pristine CF and GF suffer from relatively high electrical resistivity [9], lack of desired pore structure [24], and low specific surface area ($< 2\,m^2\,g^{-1}$) [25], which are crucial factors for efficient H_2O_2 production. Thus, they need to be further activated [24, 26, 27], pretreated [21], or modified [28].

Recently, hierarchical porous carbons proved themselves as efficient electrode materials in different areas, including HEF [29, 30]. Yet, most synthesized carbons are powdery and need further preparation to represent a freestanding geometry, which can then be used as an electrode. In this case, the powdered catalyst-containing carbon must be mixed with a polymeric binder to make a paste, and then the paste is pressed on a metal basis as a current collector to function as an electrode. These electrode preparation steps, besides being time- and energy-consuming, pose two issues. First, polymeric binders could block catalytic sites of carbon and immobilized catalysts, decreasing the final product's activity compared to that of the initial raw materials. Second, pressing carbon on a rigid metal surface may damage the carbon's inner porosity, impairing the final electrode's electroactive surface area because of the collapsed pores. More importantly, for environmental applications like HEF, the addition of polymeric binders, which are commonly fluorinated compounds like polytetrafluoroethylene (PTFE) and polyvinylidene fluoride (PVDF), may cause secondary pollution [9, 11] due to

the release of extremely persistent, highly mobile, and toxic polyfluorinated compounds [31, 32]. Therefore, developing freestanding Fe-immobilized carbons, which can directly serve as an electrode, can address these issues besides being more environmentally friendly.

Toward developing a binder-free electrode for HEF, we have lately introduced freestanding carbon microtubes (CMT) made of carbon nanotubes (CNT) in which Fe_3O_4 nanoparticles are entrapped inside the CNT matrix without any chemical binding through an infiltration step [9]. Fe_3O_4-containing CMTs proved to degrade carbamazepine (CBZ) at both pH 3 and pH 7 with outstanding reusability over consecutive cycles [9]. Additionally, the role of the 3D CNT network in both CBZ mineralization and decreased Fe leaching due to increased local pH was demonstrated [9]. Nonetheless, the use of CNTs as effective carbon materials for environmental applications, especially water/wastewater treatment, has to be carefully considered because of potential concerns of CNT's toxicity in humans, animals, and plants [33–35], which may happen due to possible undesired releases. Alternatively, Zhao et al. [18] have reported a planar freestanding Fe/Cu-coated aerogel as an efficient 3D cathode applicable over a wide range of pH 3-9 to remove methylene blue. The Fe/Cu-coated aerogel was synthesized after several curing steps of the initial precursor solution using the petrochemical and commonly-used precursors resorcinol and formaldehyde [18]. The dry gel was then carbonized under N_2 at 950 °C, activated under CO_2 at 850 °C, and treated again by reductive carbon through a calcination step under N_2 at 950 °C [18]. Hence, the synthesis method is time- and energy-intensive. Further research to develop one-pot synthesized metal-containing carbons with renewable precursors and

energy-efficient routes is required to synthesize binder-free electrodes , particularly for clean water supply via HEF. Such binder-free and self-standing carbons can bridge the gap between nano-sized catalysts development and macro-sized electrode assembly for HEF, facilitating the direct implementation of newly developed materials into tangible flow-through cells for real-life applications [9].

This study introduces a one-pot synthesized Fe-incorporated, rod-shaped carbon as an efficient electrode for HEF. The synthesis method uses bio-based precursors (sucrose and chitosan), employs ice- and silica-templating for macro and mesoporosity, respectively, and combines carbonization and activation steps with no activating agents [36]. Adding catalysts does not impose additional steps on the synthesis method, showing its versatility. As-synthesized monolithic carbon serves directly as electrodes without adding fluorinated polymeric binders to remove sulfamethoxazole (SMX) and carbamazepine (CBZ) as two recalcitrant and frequently-detected OMPs. From a scaling-up perspective, the electrode's area can versatilely be enlarged by the numbering-up of monolithic carbons for decentralized clean water supply using a flow-through module. After illustrating the capability of carbon electrodes to generate H_2O_2 and discussing the impact of applied potential and ice-templated macropore network, the reactivity of Fe catalysts incorporated into binder-free electrodes is demonstrated over consecutive runs in both acidic and neutral mediums. Moreover, the impact of CBZ and SMX properties, e.g., hydrophobicity and charge, on their transport mechanisms (pore diffusion and surface diffusion) within the ice-templated pore network of the synthesized electrodes are discussed at both pH 3 and 7.

2. Materials and Methods

2.1. Materials

High molecular weight (HMW) chitosan, sucrose (≥99 %), magnetite (Fe_3O_4) nanopowder with average particle size of 50-100 nm, acetic acid (≥99 %), sulfuric acid (99.5-99.7 %), sodium sulfate (≥99 %), and conductive glue (Leit C) were purchased from Sigma Aldrich. Colloidal dispersion of silicon dioxide (SiO_2) in water (40 %) with a particle size of 20 nm, carbamazepine (≥98 %), sulfamethoxazole (≥98 %), and titanium wires (≥99.7 %) were bought from Alfa Aesar. Sodium hydroxide (≥98 %) was supplied by Carl Roth.

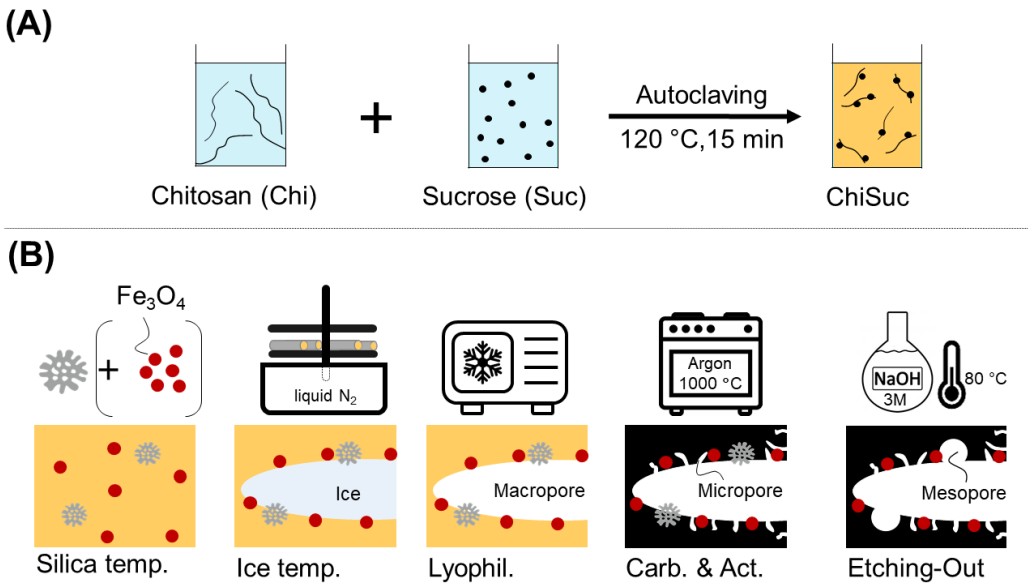

FIGURE 1: Schematic representation of precursor preparation (A) and all fabrication steps along with the pore formation in each step during the synthesis (B) for as-synthesized monolithic carbons.

2.2. Synthesis and Characterization of Monolithic Carbons

Monolithic carbons without catalyst were prepared through hard- (silica) and ice-templating combined with one-step carbonization and activation, as described in detail elsewhere [36]. Briefly, 0.3 g HMW chitosan stock solution was mixed with 0.3 g sucrose dissolved in 10 mL deionized (DI) water and placed in an autoclave for 45 min at 120 °C, including 15 min reaction and 15 min for each of the heating-up and cooling-down steps. Then, 0.3 g colloidal silica was added to the yellowish solution obtained after autoclavation and mixed vigorously before ice-templating or freeze-casting. Unlike our previous work [36], horizontal freezing of the precursor in Al molds (inner diameter of 10 mm) was considered, as photographed in Fig. S3A, to assess scaling-up feasibility for longer monolithic carbons. After lyophilization, the composite was carbonized under an argon atmosphere at 1000 °C for three hours. The carbonized sample was etched-out overnight at 85 °C in 3 M NaOH solution to remove the silica particles and create mesoporosity. This sample is named ChiSuc.

For catalyst-incorporated monolithic carbons, a certain amount of Fe_3O_4 was weighed and added to the precursor solution before freeze-casting and together with colloidal silica, imposing no additional steps to the synthesis method. All other steps remained similar, and the sample is named Fe@ChiSuc. Fig. 1 shows precursor preparation and fabrication steps schematically.

Ice-templated macroporous network, catalyst distribution, and elemental mapping of as-synthesized monoliths before and after carbonization were analyzed by scanning electron microscopy (SEM, Hitachi TM3000), Field Emis-

sion Scanning Electron Microscopy (FESEM, Hitachi S4800), and Energy Dispersive X-ray (EDX, Hitachi TM3030plus), respectively. N_2-physisorption analysis at 77 K (ASAP 2000, Micrometics) evaluated micropore and mesopore content of the final carbons. All samples were degassed at 250 °C for 24 h before measurement. The specific surface area and pore size distribution (PSD) were calculated based on the Brunauer–Emmett–Teller (BET) method and the density functional theory (DFT), respectively, as recommended for micro- and mesoporous carbons [37].

2.3. Electrochemical Experiments

Experiments for H_2O_2 production were performed in an open divided H-cell separated by a cation exchange membrane to avoid any possible oxidation of the produced H_2O_2 on the anode surface (Fig. S3C). The H-cell was equipped with a titanium mesh coated with platinum (40 cm^2) and a $Hg/HgSO_4$ (−0.68 V vs. SHE) as counter and reference electrodes, respectively. As-synthesized ChiSuc and $ChiSuc_{no–silica}$ functioned as working electrodes or cathodes. For serving as an electrode, a titanium wire with an appropriate length was covered with conductive glue (Leit-C) and inserted carefully into the final carbon for electrical connection. A shrinking tube was also used to avoid any contact between the electrolyte and the titanium wire during the electrochemical experiments, as shown in Fig. S3B. The geometrical surface area of the working electrode (ChiSuc and $ChiSuc_{no–silica}$) varied between 2.2 and 3.1 cm^2. However, the obtained results were normalized by the surface area of the corresponding electrode for a better comparison. 100 mL of 50 mM Na_2SO_4 solution adjusted to pH 7.0 ± 0.5 and pH 3.0 ± 0.1 with the help of 0.1 mM H_2SO_4 and 0.1 mM NaOH served as the catholyte.

The anolyte was 100 mL of 50 mM Na_2SO_4 solution for experiments at pH 7.0, and it was changed to 100 mL DI water set to pH 2.5 with H_2SO_4 (no salt added) for experiments at pH 3.0 to keep the catholyte's pH constant [38]. Pure O_2 was supplied with a flow rate of 90 mL min^{-1} for 10 min prior to and during each experiment.All applied potentials are reported vs. SHE, unless otherwise mentioned.

HEF treatment of CBZ and SMX was carried out in an open, undivided cell using Fe@ChiSuc with 25 mg added Fe_3O_4 nanoparticles and a geometrical surface area of 4.4 ± 0.1 cm^2 as the working electrode. The electrolyte was 100 mL of 50 mM Na_2SO_4 solution containing 4.5 ± 0.2 mg L^{-1} CBZ or SMX adjusted to pH 7.0 ± 0.5 and pH 3.0 ± 0.1. For HEF treatment of SMX in a divided H-cell, the above-described electrolyte solution was used as the catholyte, and DI water (no salt added) set to pH 2.5 and pH 3.0 served as the anolyte for experiments at pH 3 and pH 7, respectively. The contribution of direct anodic oxidation and (electro-)adsorption of CBZ on Fe@ChiSuc was assessed by saturating the solution with N_2 (90 mL min^{-1}) to avoid any H_2O_2 production and subsequent radical formation. Additionally, the role of H_2O_2 on CBZ removal was distinguished using ChiSuc as the working electrode.

For consecutive runs, the used electrode after each run was collected and thoroughly rinsed with 150 mL DI water before the next run, unless otherwise mentioned. All experiments (except consecutive runs) were performed in duplicates and reported by the average value with the standard deviation as error bars.

2.4. Analytical Methods

H_2O_2 concentrations at certain time intervals were determined spectrophotometrically at 450 nm, using a Genesys 10S UV-Vis, based on the formation of peroxovanadium cations by the ammonium metavanadate reaction with H_2O_2 in an acidic solution [39].

During the HEF, CBZ and SMX concentrations were quantified by a high-performance liquid chromatography (HPLC) system (Agilent 1100) coupled with a photodiode array detector (Agilent) at $\lambda = 285$ nm and $\lambda = 265$ nm, respectively. A LiChrospher 100 RP-18 column (250 mm x 4.0 mm, 5 µm, Phenomenex) was thermostated at 35 °C during the analysis while samples were kept at 15 °C. The pressure of the column and the flow rate of the mobile phase, being water containing 0.1% formic acid as eluent A and acetonitrile as eluent B, was set to 100 bar and 600 µL min, respectively. The volumetric ratio of eluent A/eluent B was held at 90/10 for two minutes, followed by a change to 35/65 in 9 min and from 35/65 to 5/95 in four minutes. Finally, the ratio was returned to the initial conditions in four minutes.

At the end of HEF experiments, the amount of leached iron was analyzed through inductively coupled plasma optical emission spectroscopy (ICP-OES Varian 720).

3. Results and discussion

3.1. Characterization of Freestanding Carbons

All precursors (ChiSuc, $\text{ChiSuc}_{\text{no–silica}}$, and Fe@ChiSuc) were frozen in Al molds while being placed horizontally on the freezing plate as illustrated

in Fig.1. A horizontally-placed mold offers faster freezing than a vertically-placed one [36] and addresses the issues concerning the temperature gradient for longer monoliths fabrication, which is crucial from a scale-up perspective. However, asymmetric freezing might be induced, which possibly affects the aimed radial freezing. Infrared (IR) imaging using a thermographic camera (Fig. S1) revealed that symmetrical radial freezing occurred during ice-templating. Based on Fig. S1A-C, the freezing radially proceeds from the outer edge toward the center over time. The side view images (Fig. S1D-F) confirm the symmetrical freezing along the mold's length and an outside-in freezing direction. Therefore, longer monolithic carbons can be synthesized by freezing horizontally with no concerns about the different freezing rates along the mold's length. Nonetheless, increasing the geometrical surface area of monolithic carbons by elongating molds must be thoroughly investigated, which is out of the scope of this work. Longer composites may encounter undesired and drastic shrinkage during lyophilization because of an enhanced mass transfer resistance for water sublimation. It is worth noting that the primary scaling-up strategy using as-synthesized monolithic carbon is numbering up, making an array of cylindrical carbons for larger surface areas.

Fig. 2A-C displays the SEM images of the ChiSuc 3D macroporous network formed during ice-templating. A radial and symmetrical ice-templating can be observed all over the cross-section (Fig. 2A), as expected based on IR imaging analysis (Fig. S1). However, the size of pores differs from the outer edge toward the center of carbon (Fig. 2B & C). A thin layer of small and chaotic pores on the peripheral edge of carbon is followed by the bigger pores with a lamellar structure towards the center. These observations result from

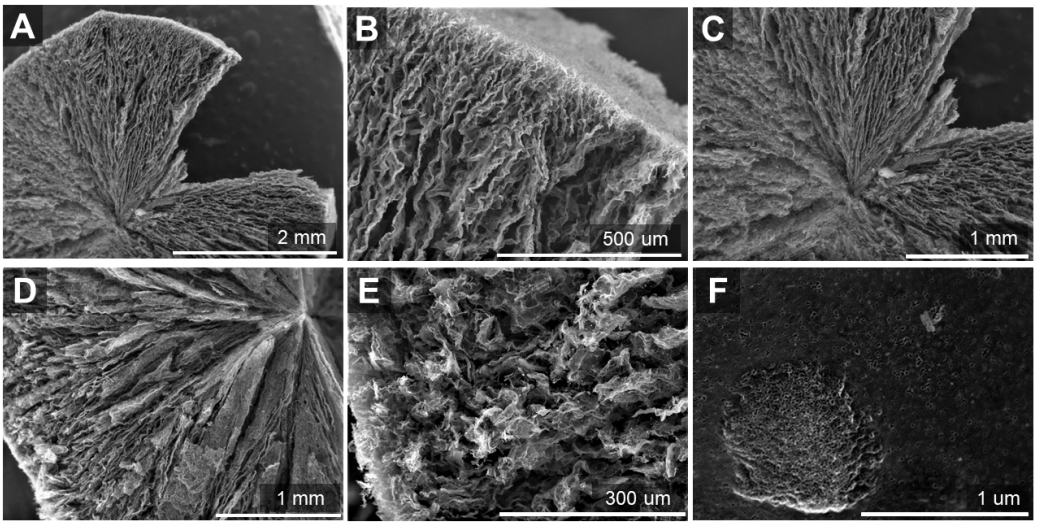

FIGURE 2: SEM images of ChiSuc (A-C) and Fe@ChiSuc (D & E) cross-section and the magnified FESEM image of ChiSuc, showing the ice-templated macropore network and silica-templated mesopores, respectively.

the difference in freezing rate. Fast freezing is expected on the peripheral edge as it is in direct contact with the Al mold. The temperature gradient decreases toward the center of the mold, causing a slowed-down freezing rate. A fast freezing rate induces ice nucleation rather than ice growth, leading to small and random ice-templated macropores. In contrast, a slow freezing rate causes the growth of already formed ice nuclei, resulting in bigger ice-templated pores with a lamellar structure. The same radial ice-templated structure can be observed after adding Fe_3O_4 nanoparticles as catalysts for Fe@ChiSuc according to Fig. 2D. However, Fe@ChiSuc possesses relatively bigger pores on the peripheral edge (Fig. 2E) compared to ChiSuc (Fig. 2B). In Figure 2F, the silica-templated mesopores all over the surface of a macro-

pore's wall can be observed.

Catalyst distribution in Fe@ChiSuc was assessed using FESEM analysis, being presented in Fig. 3. As mentioned before, no additional steps were considered for catalyst incorporation, and the Fe_3O_4 nanoparticles (50 to 100 nm) were added as catalysts with colloidal silica and well stirred before ice-templating. Fig. 3A & D display the catalyst distribution in the Fe@ChiSuc composite before carbonization. Accordingly, Fe_3O_4 nanoparticles form big agglomerates during the synthesis because of their high surface energy [17] and magnetic features. Nevertheless, after carbonization, the agglomerates have been distributed all over the surface, being distinguished as bright spots in Fig. 3B & C and the corresponding magnified images of Fig. 3E & F. The average size of bright spots increases from 60 nm (Fig. 3E) to 200 nm (Fig. 3F) by increasing the Fe_3O_4 content from 2.8 wt% to 5.5 wt%, respectively. Distribution of big Fe_3O_4 agglomerates (Fig. 3A) all over the carbon surface during carbonization can be associated with surface diffusion of particles due to their high mobility at 1000 °C. These results point out the synthesis method's facileness for producing well-distributed metal-incorporated carbons without any additional steps imposed to the fabrication procedure.

Moreover, two other characteristics are noticeable at Fe@ChiSuc after carbonization: (i) the altered shape of catalyst particles from cubic/spherical form (Fig. 3D) to oval (Fig. 3E & F), and (ii) the presence of small pores in proximity of the bright spots (Fig. 3E & F), which are clearly visible at the higher Fe_3O_4 content of 5.5 wt% (Fig. 3F). These pores are much bigger than silica-templated mesopores, which are visualized in Fig. 2F, and can

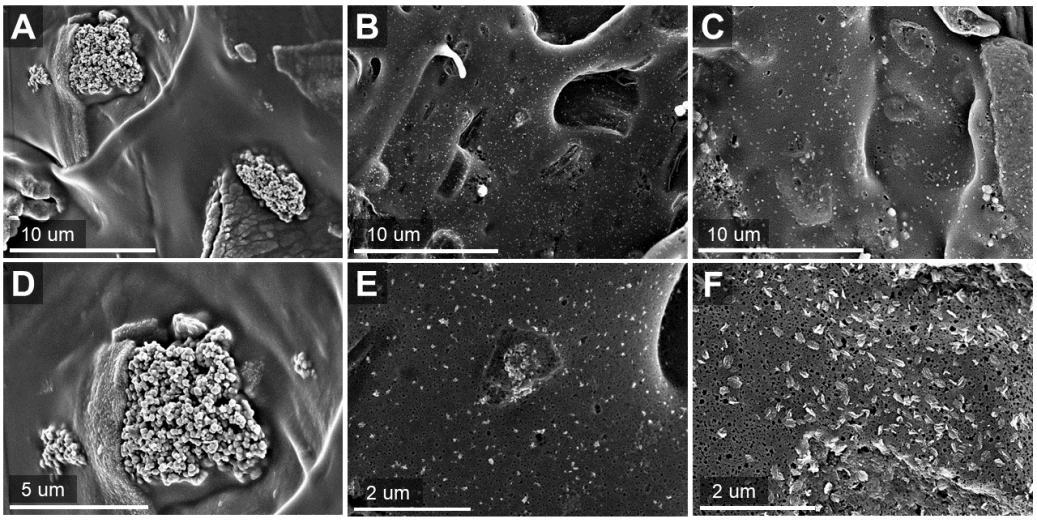

FIGURE 3: FESEM images of Fe@ChiSuc (x % added Fe_3O_4): A & D) Fe@ChiSuc (4.2 %) before carbonization; B & E) Fe@ChiSuc (2.8 %) after carbonization; and C & F) Fe@ChiSuc (5.5 %) after carbonization.

be observed neither at Fe@ChiSuc before carbonization (Fig. 3D) nor at the ChiSuc surface after carbonization (Fig. 2F). This indicates that these pores have formed during carbonization in the presence of Fe_3O_4 nanoparticles, which can be associated with the oxidation of carbon by the oxygen of Fe_3O_4 at high temperatures. Zhao and co-workers have reported the conversion Fe_3O_4 to Fe^0, or zero-valent iron (ZVI), during an activation step under N_2 at 950 °C, based on Eq.1 [18]. Thus, the incorporated catalyst differs after carbonization from the initial Fe_3O_4, which may explain the change in the catalyst's shape before and after carbonization. Energy dispersive X-ray (EDX) analysis also confirms that the oxygen content qualitatively decreases after carbonization by comparing Fig. S2C and Fig. S2F. Besides, the oxygen content in the proximity of Fe-detected spots drastically declined consider-

ing the oxygen and Fe mapping images before (Fig. S2B & C) and after (Fig. S2E & F) carbonization. The reduction of Fe_3O_4 during carbonization could benefit the reactivity of the catalyst for the Fenton chemistry. Costa et al. [40] have investigated the impact of Fe^0/Fe_3O_4 ratio by reducing Fe_3O_4 at high temperature under H_2 atmosphere. Accordingly, the highest H_2O_2 decomposition rate and methylene blue removal efficiency were achieved by the composite containing 47 % Fe^0, superior to those achieved by pure Fe^0 and pure Fe_3O_4 catalysts [40]. Additionally, both Fe_3O_4 and Fe^0 are regarded as the most reactive catalysts for HEF [4], and hence reduction during carbonization might not adversely affect the reactivity of catalysts.

$$Fe_3O_{4(s)} + 2\,C_{(s)} \longrightarrow 3\,Fe_{(s)} + 2\,CO_{2(g)} \tag{1}$$

Fig. 4 displays the N_2-physisorption analysis data of ChiSuc, $ChiSuc_{no\text{–}silica}$, and Fe@ChiSuc. According to Fig. 4A, both ChiSuc and Fe@ChiSuc contain microporosity and mesoporosity because of the sharp N_2 uptake at low relative pressures and the specific hysteresis at higher relative ones, respectively [37]. In contrast, $ChiSuc_{no\text{–}silica}$ only contains microporosity as no silica was used during the synthesis. The corresponding PSD graph (Fig. 4B) reveals a distinct peak at 12.6 nm for Fe@ChiSuc, which is slightly right-inclined for ChiSuc, centered at 17.2 nm, and is absent for $ChiSuc_{no\text{–}silica}$. This peak relates to silica-templated mesopores formed after the etching-out step.

Although the same amount of colloidal silica was added in both ChiSuc and Fe@ChiSuc recipes, the peak for Fe@ChiSuc compared to ChiSuc is three times higher, indicating that NaOH could remove more silica particles during the etching-out step (Fig. 1). This implies that the 3D ice-templated

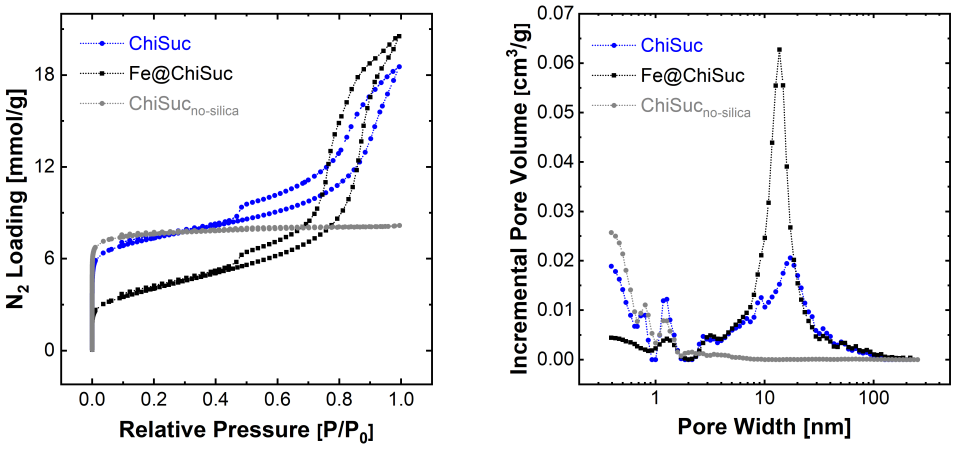

(A) (B)

FIGURE 4: N_2-physisorption analysis of ChiSuc, $ChiSuc_{no–silica}$, and Fe@ChiSuc. A) N_2-adsorption/desorption isotherms of final carbons at 77 K; B) corresponding pore size distribution (PSD) based on the DFT model for slit-shaped pores. All the samples were degassed at 250 °C for 24 h.

network of Fe@ChiSuc represents a more open and interconnected structure than ChiSuc, which is beneficial for facilitated accessibility of NaOH toward

TABLE 1: BET specific surface area, pore volume, the percent of shrinkage, and outer diameter (OD) for ChiSuc, $ChiSuc_{no–silica}$, and Fe@ChiSuc after fabrication using different amount of nanoparticles.

	Added Nanoparticles		N_2-physisorption				
Carbon	SiO_2	Fe_3O_4	S_{BET}	V_{total}	V_{meso}	V_{micro}	Shrinkage / OD
	[mg]	[mg]	[$m^2\,g^{-1}$]	[$cm^3\,g^{-1}$]	[$cm^3\,g^{-1}$]	[$cm^3\,g^{-1}$]	[%] / [mm]
ChiSuc	300	0	553 ± 46	0.52 ± 0.02	0.35 ± 0.01	0.16 ± 0.01	55 ± 2 / 4.5 ± 0.2
$ChiSuc_{no-silica}$	0	0	607 ± 60	0.22 ± 0.03	0.01 ± 0.01	0.21 ± 0.02	60 ± 1 / 4.0 ± 0.1
Fe@ChiSuc	300	25	343 ± 35	0.67 ± 0.01	0.58 ± 0.01	0.06 ± 0.01	49 ± 1 / 5.1 ± 0.1

the inner parts of the monolithic carbon [36]. The outer diameter (OD) of ChiSuc and Fe@ChiSuc attests that ChiSuc shrank more drastically (55 %) with an OD of 4.5 ± 0.2 mm than Fe@ChiSuc (49 %) with 5.1 ± 0.1 mm (Table 1). Comparatively, $ChiSuc_{no–silica}$ shows the smallest OD of 4.0 ± 0.1 mm (60 % shrinkage), being 1 mm less than Fe@ChiSuc. Shrinking of the composites during lyophilization and carbonization indicates the deformity of the ice-templated pore network, leading to blockage or isolation of interior pores. Hence, $ChiSuc_{no–silica}$ represents a less open and interconnected pore structure.

Fe@ChiSuc contains the highest amount of added nanoparticles among the three different carbons, while $ChiSuc_{no–silica}$ has no nanoparticles (Table 1). Besides acting as hard-template (colloidal silica) and catalysts (Fe_3O_4), nanoparticles serve as binding agents during the synthesis, which helps to preserve the ice-templated network from collapse during drying and carbonization steps [41]. The collapse of the ice-templated network could also explain the slightly right-inclined peak observed for ChiSuc, since such phenomenon during lyophilization may cause coalescence of silica particles, resulting in a bigger pore width (17.2 nm). The average of total pore volume (V_{total}) increases from 0.22 ± 0.03 $cm^3\,g^{-1}$ for $ChiSuc_{no–silica}$ to 0.52 ± 0.02 $cm^3\,g^{-1}$ and 0.67 ± 0.01 $cm^3\,g^{-1}$ for ChiSuc and Fe@ChiSuc, respectively, due to the increased mesoporosity (V_{meso}).

$ChiSuc_{no–silica}$, despite containing no mesoporosity, shows the highest micropore volume (V_{micro}) with an average of 0.21 ± 0.02 $cm^3\,g^{-1}$. Since micropores significantly raise the specific surface area of porous materials, $ChiSuc_{no–silica}$ offers the highest average of BET specific surface area (S_{BET}) of $607 \pm$

60 $m^2\,g^{-1}$ followed by 553 ± 46 $m^2\,g^{-1}$ (V_{micro}= 0.16 ± 0.01 $cm^3\,g^{-1}$) and 343 ± 35 $m^2\,g^{-1}$ (V_{micro}= 0.06 ± 0.01 $cm^3\,g^{-1}$) for ChiSuc and Fe@ChiSuc, respectively. Micropores form during carbonization once inherently less stable functional groups leave the carbon surface at high temperatures [42, 43], which, in this work, occurs on the wall of ice-templated macropores (Fig. 1) [36]. Hence, the drastic decline in V_{micro} for Fe@ChiSuc compared to ChiSuc can be associated with the oxidation of the carbon surface, occurring during carbonization due to the oxidative environment caused by Fe_3O_4 presence. This oxidation of the carbon surface leads to the formation of relatively big pores in the proximity of catalyst particles (Fig. 3E & F), as discussed earlier, destroying the micropores formed or forming on the ice-templated macropores. Therefore, $ChiSuc_{no-silica}$, ChiSuc, and Fe@ChiSuc are characterized as microporous, micro-/mesoporous, and mesoporous monolithic carbons, respectively.

3.2. Electro-generation of H_2O_2 by ChiSuc (pH 7)

The capability of as-synthesized monolithic carbons for electro-generation of H_2O_2 is demonstrated through a set of experiments conducted in a divided cell at different applied potentials, and the results are presented in Fig. S4 and Fig. 5A. Fig. S5 shows the monitored current density over time at 0.13 V, -0.02 V, -0.17 V, and -0.47 V vs. SHE, showing an average steady current density (Fig. S5, inset) of 0.44 ± 0.01 $mA\,cm^{-2}$, 1.1 $mA\,cm^{-2}$, 1.2 $mA\,cm^{-2}$, and 1.4 ± 0.1 $mA\,cm^{-2}$, respectively. It has to be mentioned that the presence of Fe in Fe@ChiSuc may promote the further reaction of H_2O_2 to radicals, leading to a decreased H_2O_2 concentration during electrolysis. Thus, ChiSuc was selected as the cathode for these experiments.

At a potential of 0.13 V, the average of specific production rate is 0.08 mg cm^{-2} h^{-1} with a current efficiency (CE) of $25 \pm 1\%$ and it reaches 0.21 mg cm^{-2} h^{-1} at -0.02 V without any significant change of CE ($26 \pm 2\%$). Further decrease of the cathodic potential to -0.17 V led to an even higher production rate of 0.3 mg cm^{-2} h^{-1} with the highest achieved CE of $33 \pm 2\%$, but it drastically declined to 0.12 mg cm^{-2} h^{-1} at -0.47 V with a significantly impaired CE of $11 \pm 1\%$. The low specific production rate at 0.13 V relates to the insufficient cathodic potential at the electrode's surface to reduce available O_2 to H_2O_2 (Eq. 2). However, the declined production rate at the highest cathodic potential of -0.47 V comes from the low solubility of oxygen, being a limiting factor at the electrode's surface [36], and the presence of parasite reactions, e.g., Eq. 3, Eq. 4, and Eq. 5.

$$O_{2(g)} + 2\,H^+ + 2\,e^- \longrightarrow H_2O_2 \tag{2}$$

$$H_2O_2 + 2\,H^+ + 2\,e^- \longrightarrow 2\,H_2O \tag{3}$$

$$O_{2(g)} + 4\,H^+ + 4\,e^- \longrightarrow 2\,H_2O \tag{4}$$

$$2\,H^+ + 2\,e^- \longrightarrow H_{2(g)} \tag{5}$$

These results demonstrate the capability of monolithic ChiSuc for serving directly as a binder-free electrode to produce H_2O_2 on-site. It has to be noted that the specific production rate achieved in this study cannot be directly compared with the literature [17, 44–47], where the final synthesized

carbon was used as powders, mixed with polymeric binders, and fixed as a thin layer (several µm) on a current collector to serve as an electrode. Table S1 represents the H_2O_2 production rate and CE (if data was available) of different commercial and in-house synthesized freestanding carbons with no added polymeric binder.

commercial carbons such as graphite [48], graphite felt [49, 50], carbon felt [51], carbon sponge [51], and reticulated vitreous carbon (RVC) foam [52] have been widely used as cathodes for H_2O_2 production and pollutants degradation via electro-Fenton. For these cathodes, the H_2O_2 production rate varies from $0.03\,\mathrm{mg\,cm^{-2}\,h^{-1}}$ for graphite to $1.84\,\mathrm{mg\,cm^{-2}\,h^{-1}}$ for carbon sponge, depending upon the properties of carbonaceous cathodes themselves and operational conditions. Comparatively, ChiSuc yielded to a H_2O_2 production rate of $0.3\,\mathrm{mg\,cm^{-2}\,h^{-1}}$, which lies in the range of commercial carbon electrodes. It has to be noted that the H_2O_2 rate for ChiSuc was calculated based on its peripheral surface; whereas, the values reported in the literature are based on one side of the electrode's surface, which increases the production rate. Considering half of the geometrical surface area of ChiSuc, the specific production rate for cylindrical ChiSuc at a constant cathodic potential of $-0.17\,\mathrm{V}$ (current density of $1.2\ \mathrm{mA\,cm^{-2}}$, Fig. S5) is $0.6\,\mathrm{mg\,cm^{-2}\,h^{-1}}$, being around one-third of the maximum value ($1.84\,\mathrm{mg\,cm^{-2}\,h^{-1}}$) achieved by a carbon sponge at a remarkably higher current density of $16.1\ \mathrm{mA\,cm^{-2}}$ [51].

One credible explanation for the relatively low specific production rate achieved by ChiSuc, despite having a hierarchical porosity and heteroatoms content, can be attributed to the 3D porous network of the electrode. The

ChiSuc monolith with an OD of 4.5±0.2 mm serves as the electrode, meaning that the H_2O_2 produced on the inner carbon surface inside the 3D macroporous network must move outside of the carbon matrix to be measured during experiments. The openness of the 3D porous network significantly matters for two aspects: first, the transport of dissolved O_2 from the bulk electrolyte toward the reaction sites at the electrode's surface, and second, the transport of the formed H_2O_2 back toward the bulk electrolyte, where it can be measured. If the transport path for H_2O_2 is narrow with high tortuousness, it cannot be influenced by the convective flow induced by mixing, and hence, it occurs via diffusion. Such diffusion happens along the carbonaceous channels of the electrode that may promote further electro-reduction of H_2O_2 to water (Eq. 3) before reaching out to the bulk electrolyte [5].

The electro-reduction of H_2O_2 is closely related to the cathode's structure. If the cathode's structure is non-porous, there is no H_2O_2 entrapment inside a 3D pore network to be further electrochemically reduced to water. Zhou and co-workers [52] have systematically assessed the effect of a porous network on the extent of H_2O_2 electro-reduction using a non-porous graphite plate and a porous RVC foam, illustrating a much faster H_2O_2 electro-reduction on the RVC foam surface than on non-porous graphite [52].

In comparison to in-house synthesized freestanding carbons (Table S1), ChiSuc resulted to a higher CE (33 %) and H_2O_2 production rate ($0.3\,mg\,cm^{-2}\,h^{-1}$) than a carbon aerogel (18 %) [53] and N-enriched graphitic carbon ($0.07\,mg\,cm^{-2}\,h^{-1}$) [54], respectively. Wang et al. [53] has reported a H_2O_2 production rate of $0.23\,mg\,cm^{-2}\,h^{-1}$ for the inactivated carbon aerogel ($S_{BET} = 744\,m^2\,g^{-1}$), while it increased to $0.82\,mg\,cm^{-2}\,h^{-1}$ for the activated one ($S_{BET} = 2417\,m^2\,g^{-1}$),

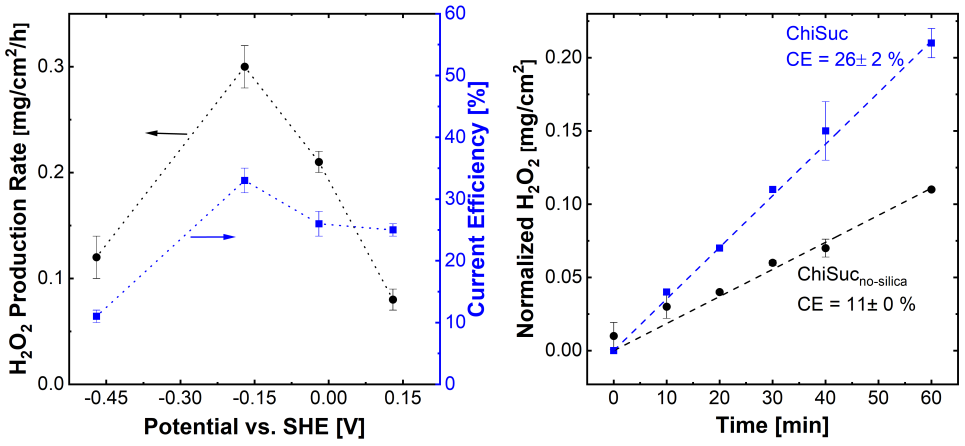

(A) (B)

FIGURE 5: Electro-generation of H_2O_2 in an open divided H-cell: 50 mM Na_2SO_4 (100 mL) as catholyte, pH_0 7.0 ± 0.5. A) Effect of the applied cathodic potential on the specific H_2O_2 production rate and current efficiencies using ChiSuc as the cathode; B) Normalized (per geometrical surface area of the electrode) H_2O_2 production at −0.02 V over one-hour electrolysis for ChiSuc and $ChiSuc_{no–silica}$ with their associated current efficiency (CE).

despite having higher specific surface areas than monolithic ChiSuc, especially after activation.

.

To further illustrate the crucial role of the 3D ice-templated network on H_2O_2 concentrations in the bulk solution, a set of experiments at −0.02 V was conducted with $ChiSuc_{no–silica}$ as the cathode. As discussed earlier, $ChiSuc_{no–silica}$ has the smallest OD of 4.0 ± 0.1 mm, showing the most drastic shrinkage because of no nanoparticles added. According to Fig. 5B, the specific production rate for $ChiSuc_{no–silica}$ is 0.11 mg cm^{-2} h^{-1} after one hour,

being half of the value achieved for ChiSuc ($0.21\,\mathrm{mg\,cm^{-2}\,h^{-1}}$), despite showing a comparable specific surface area (Table. 1) and a slightly higher amount of transferred charge (13 ± 1 C compared to 11 ± 1 C for the ChiSuc) during the experiment. This lower specific production rate declined the CE to 11 % for $\mathrm{ChiSuc_{no\text{–}silica}}$ even though the only difference in ChiSuc and $\mathrm{ChiSuc_{no\text{–}silica}}$ recipes is the presence of colloidal silica as hard-templates. Hence, it can be deduced that the more shrunk and collapsed structure of $\mathrm{ChiSuc_{no\text{–}silica}}$ has caused a hampered mass transfer of the produced H_2O_2 toward the bulk solution.

To minimize the influence of the ice-templated pore network on H_2O_2 mass transfer, the monolithic $\mathrm{ChiSuc_{no\text{–}silica}}$ was ground. The powdered $\mathrm{ChiSuc_{no\text{–}silica}}$ was coated on a rotating ring disk electrode (RRDE) setup (experimental details in supporting information). Fig. S6 shows the corresponding results for H_2O_2 selectivity, or CE, over a wide potential range. In this case, the CE varies between 51 ± 14 % to 23 ± 8 % by decreasing the cathodic potential from 0.6 V vs. RHE to 0.05 V vs. RHE. In H-cell experiments at pH 7.0 ± 0.5, the pH of catholyte increased to 11.2 ± 0.3, meaning that the applied cathodic potential (-0.02 V vs. SHE) was initially 0.39 V vs. RHE and increased to 0.64 V vs. RHE due to the pH shift after one-hour electrolysis, with an average value of 0.52 V vs. RHE.

The RRDE experiments show a H_2O_2 selectivity, or CE, of 37 ± 11 % for powdered $\mathrm{ChiSuc_{no\text{–}silica}}$ at a potential of 0.52 V vs. RHE, which is more than three times higher than that achieved by monolithic $\mathrm{ChiSuc_{no\text{–}silica}}$ (Fig. S6). Hence, the ice-templated pore network deteriorates the H_2O_2 mass transfer toward the bulk solution, being beneficial for a HEF process, where the

electro-generated H_2O_2 must react with adjacent catalysts to produce radicals. Additionally, a 3D ice-templated network could be beneficial for the mineralization of organic pollutants as it provides temporary confinement of oxidation by-products close to the catalytic sites [9].

3.3. Carbamazepine Removal by Fe@ChiSuc (pH 7)

A set of experiments was conducted to remove carbamazepine (CBZ), a frequently detected micropollutant in water bodies [9], in order to prove the catalytic activity of as-synthesized Fe@ChiSuc. CBZ is an anticonvulsant and cannot be degraded by H_2O_2 solely, given its chemically persistent nature [9, 17]. It represents a suitable model compound to prove the activity of Fe@ChiSuc as a potential electrode for HEF to produce radicals. Fig. 6A displays the results of CBZ removal at pH 7 under different experimental conditions in an undivided cell.

Accordingly, a negligible amount of CBZ was removed under N_2 bubbling at $-0.17\,\mathrm{V}$ as cathodic potential. Under such oxygen free conditions, the HEF oxidation mechanism is suppressed , while two other possible removal mechanisms remain: (i) (electro)adsorption on porous Fe@ChiSuc, and (ii) direct oxidation on the anode surface. Based on the results, the role of (electro)adsorption and anodic oxidation at the applied cathodic potential of $-0.17\,\mathrm{V}$ is insignificant. Additionally, the experiments with ChiSuc as a cathode resulted in slightly better CBZ removal of 11 ± 2 % after 60 min, being most likely attributable to adsorption of CBZ on the much larger BET surface area of ChiSuc ($553 \pm 46\ \mathrm{m^2\,g^{-1}}$) compared to Fe@ChiSuc ($343 \pm 35\ \mathrm{m^2\,g^{-1}}$).

In contrast, when O_2 was bubbled during the experiment with Fe@ChiSuc, the CBZ concentration was significantly depleted after a one-hour experi-

ment, i.e., with Fe@ChiSuc up to 67 ± 4 % removal of CBZ was noticed with a pseudo-first-order rate constant (k) of 0.023 ± 0.002 min^{-1} (Table S2). The CBZ removal indicates the formation of radicals [9, 17], resulting from the

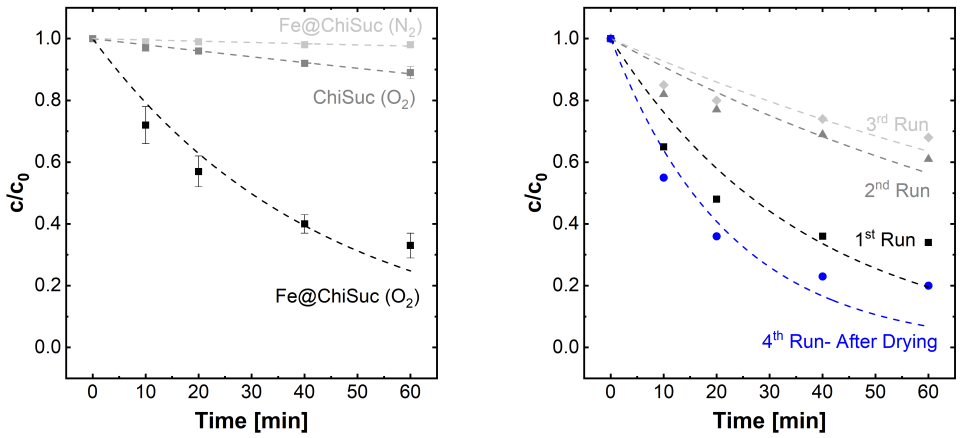

(A) (B)

FIGURE 6: CBZ decay at pH$_0$ 7.0 ± 0.5 and -0.17 V in 50 mM Na_2SO_4 (100 mL, $[CBZ]_0 = 4.5 \pm 0.2$ mg L^{-1}) using an open undivided cell. A) Different degradation mechanisms involved in which each experimental data represents an average of two experiments with the standard deviation as error bars, being fitted (dashed lines) to the pseudo-first-order kinetic model (Table S2): electro-sorption + anodic oxidation (Fe@ChiSuc under N_2 bubbling), H_2O_2 + anodic oxidation (ChiSuc under O_2 bubbling), HEF + anodic oxidation (Fe@ChiSuc under O_2 bubbling); B) Reusability of Fe@ChiSuc over four consecutive runs with one monolithic carbon under similar experimental conditions, being fitted to the pseudo-first-order kinetic model (dashed lines): after the first run with a fresh Fe@ChiSuc, the electrode was rinsed and used immediately for the second and third runs, while being rinsed and dried for the fourth run (Fig. 7A).

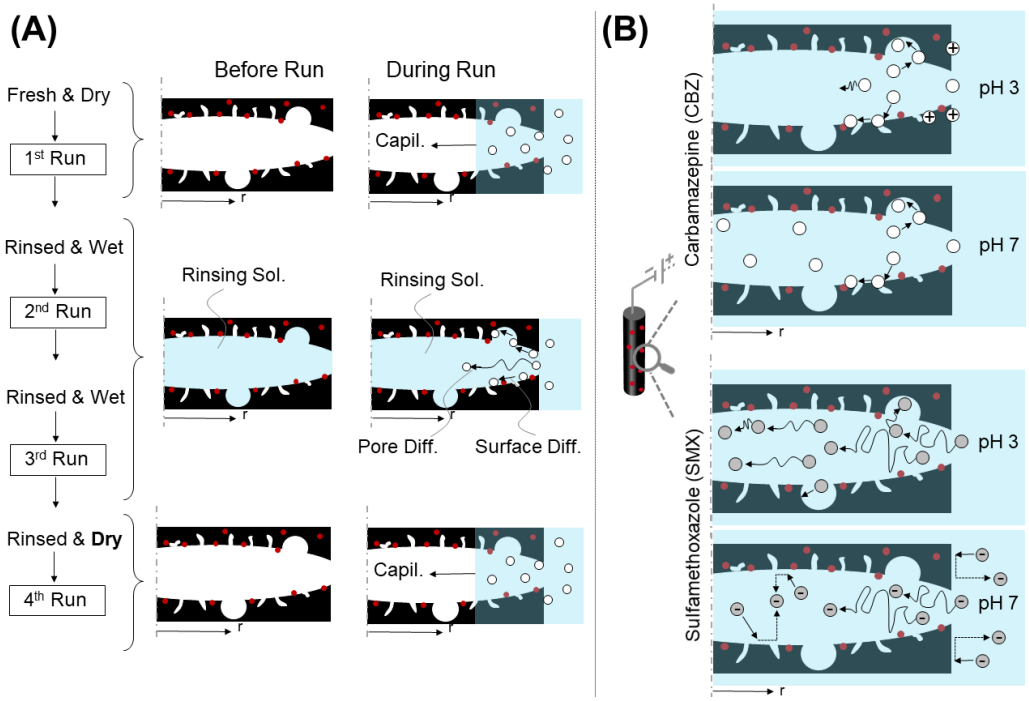

FIGURE 7: Schematic representation of an ice-templated pore with a hierarchical structure from the center of the monolithic carbon in radial direction during HEF experiments. A) Pore representation in consecutive runs with fresh, rinsed & wet, and rinsed & dry Fe@ChiSuc before and during each run; B) Sulfamethoxazole and carbamazepine properties at pH 3 and pH 7 during the HEF process.

catalytic reactions between electrogenerated H_2O_2 (Fig. 5A) and embedded catalyst particles on the Fe@ChiSuc surface. Therefore, the results demonstrate the activity of Fe@ChiSuc as a binder-free monolithic electrode for HEF processes at neutral pH.

Apart from the activity of catalysts, the reusability of Fe-containing carbons is a challenging issue for the implementation of HEF processes at larger scales [6]. Hence, the reusability of Fe@ChiSuc over four consecutive runs

was also investigated at pH 7, and the results are presented in Fig. 6B. After the first run with a fresh Fe@ChiSuc carbon, the monolith was carefully rinsed with 150 mL deionized (DI) water before the second and third runs, while it was rinsed and dried at room temperature before the fourth run, as depicted in Fig. 7A.

During the first run at pH 7, 68 % of CBZ is removed after one-hour electrolysis, followed by a sudden drop to 39 % and 32 % for the second and third run, respectively. Accordingly, the rate constant (k) declined from 0.027 ± 0.005 min^{-1} for the first run to 0.010 ± 0.001 min^{-1} and 0.008 ± 0.001 min^{-1} for the second and third run, respectively, showing a much slower ($\leq$ 2.7 times) removal rate for the successive runs. Nevertheless, Fe@ChiSuc could remove 80 % of CBZ at the fourth run with a rate constant of 0.045 ± 0.007 min^{-1}, showing even better performance than the first run. According to Table S3, the amount of leached Fe after one-hour electrolysis at the first and fourth runs is $0.02\,mg\,L^{-1}$ and $0.03\,mg\,L^{-1}$, respectively, while being lower than the detection limit for the second and third run. These results suggest that neither the iron loss nor deactivation could explain the significant drop in CBZ removal after the second and third runs.

Another perspective can be the treatment way of the used Fe@ChiSuc after each run, which was different for the fourth run compared to the second and third runs (Fig. 7A). Before the second and third runs, the used Fe@ChiSuc was rinsed with DI water and reused immediately. The rinsed carbon with an OD of 5.0 ± 0.1 mm is wet and filled with solution, occupying the porous interior network of the electrode and hindering the solution ingress by capillary forces during the next run. This implies that the CBZ

containing solution, during the second and third run, had to diffuse into the rinsing solution (Fig. 7A) to reach the catalytic sites located in the interior parts of Fe@ChiSuc, causing a dramatic decline in the CBZ removal rate. The diffusion of organic micropollutants (OMPs) into the porous network of Fe@ChiSuc may happen through surface diffusion, pore diffusion, or a combination thereof [55]. Surface diffusion is defined as the transport of adsorbed OMPs along the internal carbon surface, whereas the transport of OMPs in the liquid phase inside a pore refers to pore diffusion [55]. Hence, a higher diffusion coefficient can be expected for the pore diffusion compared to the surface diffusion as the transport of a molecule in a liquid phase is facilitated [56]. Additionally, it could be assumed that the surface diffusion is more relevant for hydrophobic compounds like CBZ (with an octanol-water partition coefficient ($LogK_{ow}$) of 2.45 [57]) than for hydrophilic ones like SMX ($LogK_{ow}$ =0.89 [57])) due to their higher adsorption affinity[58]. Therefore, the lower CBZ removal rate achieved during the second and third runs is associated with the slow transport mechanism of CBZ by surface diffusion (Fig. 7A).

On the other hand, the carbon was dried before the first and fourth runs. Thus, the CBZ containing solution could fill the whole carbon depth through capillary forces, which led to extended reaction sites for CBZ removal, as depicted in Fig. 7A. It is worth mentioning that the slightly better CBZ removal achieved at the fourth run compared to the first one can be associated with a better wetting behavior of the used Fe@ChiSuc compared to the fresh Fe@ChiSuc due to some salt deposition after three consecutive runs in 50 mM Na_2SO_4 solution [59]. The presence of salts on the carbon surface impairs the

hydrophobic characteristics of carbon, resulting in a faster contact between the electrolyte and electrode, and thus, a faster CBZ removal.

These results indicate the importance of types of carbon treatment in consecutive runs, especially when the carbon has a thickness in the mm range. For instance, Zhao and co-workers [18] presented a carbon aerogel coated with copper and iron as freestanding electrodes for HEF, demonstrating a consistent methylene blue removal efficiency for six consecutive runs. However, for reusability tests, the carbon was collected after each run, washed with DI water, and dried in a vacuum oven before the next run [18]. Nevertheless, it has to be noted that the big OD of Fe@ChiSuc is not an issue in a flow-through module, where a flow of solution would cross the monolithic Fe@ChiSuc in the direction of ice-templated macropores, providing a dynamic change of solution all over the Fe@ChiSuc depth for an efficient pollutants removal.

3.4. Carbamazepine Removal by Fe@ChiSuc (pH 3)

Fig. 8A represents the average of CBZ removal at pH 3 with fresh Fe@ChiSuc electrodes, while Fig. 8B shows the performance of one Fe@ChiSuc in an acidic medium over four consecutive runs for CBZ removal. For a better comparison, the results of CBZ removal at pH 7 were also added to Fig. 8A. For consecutive runs at pH 3, a fresh Fe@ChiSuc was used for the first run, and the electrode was thoroughly rinsed with 150 mL DI water and used for the subsequent runs without any drying. Change of pH from 7.0 ± 0.5 to 3.0 ± 0.1 alters the applied cathodic potential (-0.17 V vs. SHE) from 0.24 V vs. RHE to 0.01 V vs. RHE, and consequently decreases the anodic potential from 1.9 V vs. RHE to 1.8 V vs. RHE (average cell potential is

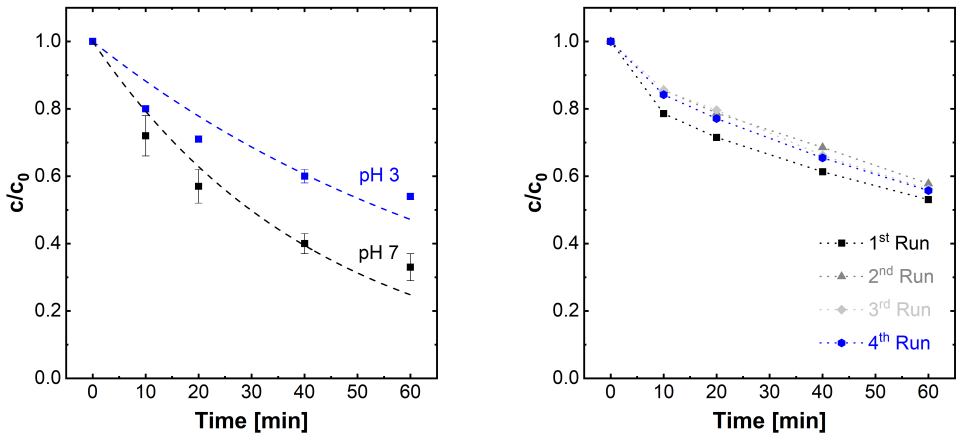

(A) (B)

FIGURE 8: CBZ decay at pH_0 3.0 ± 0.1 and $-0.17\,V$ in $50\,mM$ Na_2SO_4 ($100\,mL$, $[CBZ]_0 = 4.5 \pm 0.2\ mg\,L^{-1}$) using Fe@ChiSuc in an open undivided cell. A) The average of two different experiments with standard deviation as error bars, being fitted (dashed lines) to the pseudo-first-order kinetic model (Table S2). For comparison reasons, the values obtained at pH_0 7.0 ± 0.5 are also depicted; B) Reusability of Fe@ChiSuc over four consecutive runs with one monolithic carbon under similar experimental conditions, which are not fitted to an exponential decay model for visual reasons: after the first run with a fresh Fe@ChiSuc, the electrode was rinsed and used immediately for the other runs.

$-1.7\,V$ and $-1.8\,V$, respectively). Hence, it can be presumed that impact of anodic oxidation on CBZ removal remains negligible at pH 3.0 ± 0.1, as observed for pH 7.0 ± 0.5.

Based on Fig. 8A, Fe@ChiSuc can remove 46 ± 1 % CBZ at pH 3, which is lower than that 67 ± 4 % at pH 7, resulting to a pseudo-first-order removal rate constant of $0.013 \pm 0.001\ min^{-1}$. Based on RRDE experiments

for powdered ChiSuc (Fig. S7), H_2O_2 selectivity stays almost constant at a wide potential range (from 0.58 V vs. RHE to 0.05 V vs. RHE). Thus, the lower CBZ removal efficiency at pH 3.0 ± 0.1 cannot be primarily attributed to a decreased electro-generation of H_2O_2.

Unlike the consecutive runs at pH 7 (Fig. 6B), those at pH 3 (Fig. 8B) are more consistent and show no significant drop in efficiency despite having a similar rinsing method between runs. In this case, the CBZ removal efficiency is 47 % after the first run and slightly declines to 42 %, 44 %, and 44 % after the second, third, and fourth run, respectively. The consistency of CBZ removal rates over the consecutive runs indicates that the presence of the rinsing solution in the interior pore structure of the Fe@ChiSuc electrode influences the CBZ removal at pH 3 to a much less degree. Additionally, this implies that the capillary forces, which were dominant at neutral pH for CBZ solution ingress into the interior pores of the dry electrode, are dominated by another mechanism at pH 3. This could also explain the lower CBZ removal efficiency at pH 3 than at pH 7 (Fig. 8A). The extent of CBZ removal depends upon the catalytic sites of Fe@ChiSuc being in contact with CBZ dissolved in the electrolyte, which in turn could be contingent upon the properties of CBZ at different pH values. CBZ solubility increases from acidic solutions (pH 2) to circumneutral pH values (pH > 5) [60], being supported by its decreased octanol-water partition coefficient at pH 7.4 (LogD value) [61]. Besides that, CBZ is partially protonated at pH 3 [62]. Both factors promote CBZ adsorption on the outer carbon surface of the hydrophobic and negatively charged electrode, as depicted in Fig. 7B. Subsequently, the further transport of the adsorbed CBZ happens through surface diffusion instead of capillary forces,

as discussed earlier, which impairs the removal rate of CBZ. In contrast, the CBZ is 100 % neutral at pH 7 and has no electrostatic attraction toward the carbon surface, besides being more soluble and mobile.

Furthermore, at acidic environment, the concentration of leached Fe from Fe@ChiSuc after one-hour electrolysis is $0.06\,\mathrm{mg\,L^{-1}}$, $0.04\,\mathrm{mg\,L^{-1}}$, $0.04\,\mathrm{mg\,L^{-1}}$, and $0.1\,\mathrm{mg\,L^{-1}}$ for the first, second, third, and forth run, respectively. The extent of leached Fe distinguishes the contribution of homogeneous and heterogeneous catalysis, suggesting an absolutely heterogeneous reaction [18, 63] at both pH 3 and pH 7. It is worth noting that, at pH 3, the concentration of leached Fe is slightly lower from Fe@ChiSuc (working area of $4.4\,\mathrm{cm^2}$), with one step carbonization and activation, than the value ($\approx$$0.09\,\mathrm{mg\,L^{-1}}$) leached from FeCuC aerogel (working area of $2\,\mathrm{cm^2}$) activated in two separate and energy-intensive steps after one-hour electrolysis [18]. The negligible concentration of leached Fe from Fe@ChiSuc can be associated with the 3D ice-templated carbon network that could provide an increased local pH [64] due to proton consumption via oxygen reduction reactions (Eq. 2 and Eq. 4) and mitigate Fe leaching during electrolysis [9].

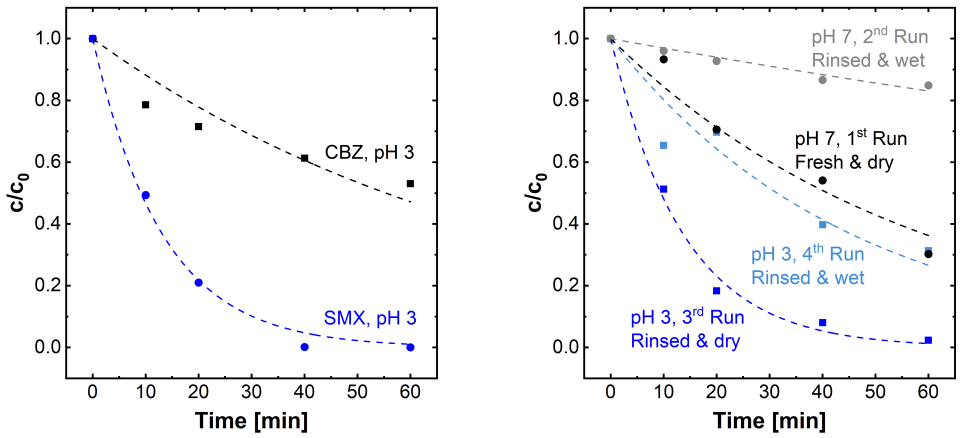

(A) (B)

FIGURE 9: Degradation experiments over one-hour runs at a cathodic potential of $-0.17\,\mathrm{V}$ using Fe@ChiSuc. A) SMX and CBZ (for comparison reasons) decay in an open undivided cell at pH_0 3.0 ± 0.1 using $50\,\mathrm{mM}$ Na_2SO_4 electrolyte ($100\,\mathrm{mL}$, $[\mathrm{SMX}]_0 = 4.5 \pm 0.2\ \mathrm{mg\,L^{-1}}$) and fresh Fe@ChiSuc monoliths, being fitted (dashed lines) to the pseudo-first-order kinetic model (Table S2) B) SMX decay in an open divided H-cell over four successive runs at pH_0 3.0 ± 0.1 and pH_0 7.0 ± 0.5 using $50\,\mathrm{mM}$ Na_2SO_4 ($100\,\mathrm{mL}$, $[\mathrm{SMX}]_0 = 4.5 \pm 0.2\ \mathrm{mg\,L^{-1}}$) as the catholyte, being fitted (dashed lines) to the pseudo-first-order kinetic model (Table S2). DI water set to pH 2.5 and pH 3.0 served as the anolyte for pH_0 3.0 ± 0.1 and pH_0 7.0 ± 0.5 experiments, respectively. A fresh Fe@ChiSuc was used for the first run, followed by the second run with the rinsed ($150\,\mathrm{mL}$ DI water) and wet electrode. After the second run, the electrode was rinsed and dried overnight for the third run, followed by the fourth run with the rinsed and wet electrode.

3.5. Sulfamethoxazole Removal by Fe@ChiSuc (pH 3 and pH 7)

Fig. 9 represents the performance of Fe@ChiSuc in removing sulfamethoxazole (SMX) as another example of persistent and commonly-detected OMPs

in water bodies. SMX is an ionizable antibiotic, which has two pK_a values (1.6 and 5.7) [56], being neutral and negatively charged at pH 3 and pH 7, respectively. Moreover, SMX is relatively hydrophilic ($LogK_{ow}$ and LogD of 0.89 [57, 61] and -0.56 [61], respectively) and shows less adsorption affinity on carbon materials compared to CBZ [65, 66], especially at such low initial concentration ($[SMX]_0 = 4.5 \pm 0.2\ mg\,L^{-1}$) and on the surface of mesoporous Fe@ChiSuc, which lacks micropores [67].

According to Fig. 9A, SMX is completely depleted after 40 min at pH 3 with a rate constant of $0.076 \pm 0.004\ min^{-1}$, which is around six times higher than the one for CBZ removal ($0.013 \pm 0.002\ min^{-1}$) at pH 3. One reason could be the contribution of direct anodic oxidation in an undivided cell because SMX is less recalcitrant than CBZ to oxidize. Garica and co-workers [68] have reported a 30 % higher pseudo-first-order rate constant for SMX removal ($0.013\ min^{-1}$) than CBZ ($0.011\ min^{-1}$) one under similar experimental conditions on the surface of a boron-doped diamond (BDD) electrode. However, this does not explain such difference obtained here. The primary difference between CBZ and SMX properties is their affinity for adsorption considering their $LogK_{ow}$ values (2.45 and 0.89 for CBZ and SMX, respectively)[58]. This influences the transport mechanism of the target pollutants inside the internal porosity of Fe@ChiSuc. Unlike CBZ, the more hydrophilic SMX transports via pore diffusion in the liquid phase rather than through surface diffusion on the solid surface (Fig. 7B). As a result, the rate constant for SMX removal is higher since more catalytic sites of Fe@ChiSuc can be reached in the oxidation of SMX during one-hour electrolysis.

In Fig. 9B, SMX removal in a divided H-cell over four successive runs (two

at pH 3 and two at pH 7) is illustrated to evaluate the effect of capillary forces. A fresh Fe@ChiSuc electrode was used for the first run at pH 7, followed by the second run under similar conditions with the rinsed and wet Fe@ChiSuc. Subsequently, the used electrode was rinsed and dried overnight and reused for the third run at pH 3, followed by the fourth run with the rinsed and wet Fe@ChiSuc under similar experimental conditions. Unlike CBZ removal experiments, SMX degradation tests were performed in a divided H-cell to omit the effect of anodic oxidation, especially at pH 7 with the promoted electrostatic forces between the negatively charged SMX and the positively charged anode's surface.

At pH 7, the constant rate for SMX removal is 0.017 ± 0.002 min^{-1} for the first run, which significantly drops to 0.003 min^{-1} for the second run with the wet electrode. The same trend can be observed at pH 3, where a higher rate constant of 0.073 ± 0.005 min^{-1} was achieved for the third run (dry Fe@ChiSuc) than that for the fourth run (0.022 ± 0.001 min^{-1}) with the wet electrode. As discussed earlier, the runs with the wet Fe@ChiSuc show a declined removal efficiency due to the lack of capillary forces and the dominance of diffusion mechanisms (Fig.7A). Although the dominant transport mechanism at both the second and fourth runs (with wet Fe@ChiSuc) is pore diffusion, the decline at the rate constant is more drastic at pH 7 (6.3 times slower than the first run) compared to pH 3 (3.3 times slower than the third run). Additionally, SMX removal rates at pH 7 are extremely lower than those at pH 3 with both dry and wet Fe@ChiSuc. Moreover, at pH 7, the removal rates for SMX, which is less recalcitrant than CBZ to oxidize [68], are lower than those for CBZ under similar conditions (Table S2).

The credible explanation for these observations is the negative charge of SMX at pH 7, being repelled from the negatively charged Fe@ChiSuc during the HEF process (Fig. 7B). During the first run, the capillary forces counteract the charge repulsion to some extent, resulting in 70 % SMX removal after one hour. However, during the second run and in the absence of capillary forces (Fig. 7A), the repulsion overcame the pore diffusion mechanism and led to an extremely impaired removal efficiency of 15 %. Therefore, it can be deduced that the molecule's charge tremendously affects the removal efficiency and rate constant in a surface-catalyzed HEF process, especially in this work with the negligible amount of leached Fe (see Table S3). Yet, it can be counteracted by stronger forces, e.g., capillary or convective forces, in a flow-through module.

Furthermore, transport mechanisms for SMX and CBZ and their impact on the corresponding removal rates can be supported by comparing the CBZ and SMX removal efficiencies using a wet Fe@ChiSuc (the diffusion predominates the capillary forces) when they are both neutral. That is, SMX at pH 3 (Fig.9B, the fourth run) and CBZ at pH 7 (Fig.6B, the second run). Based on Table S2, the constant rate for SMX and CBZ is 0.022 ± 0.003 min^{-1} and 0.010 ± 0.001 min^{-1}, respectively, being two times higher for the hydrophilic SMX. Such a difference cannot be solely explained by the recalcitrant nature of the molecules [68]. Hence, in the absence of electrostatic interactions, it could be associated with the diffusion rate of these two OMPs inside the porous ice-templated network of Fe@ChiSuc.

4. Conclusions

This study reports a novel Fe-containing freestanding carbon made of chitosan and sucrose as precursors as an effective electrode for heterogeneous electro-Fenton (HEF) processes at a wide pH range. Monolithic carbons (ChiSuc, $ChiSuc_{no–silica}$, and Fe@ChiSuc) have cylindrical geometry with a mm-ranged diameter, offering a 3D ice-templated radial pore network on which silica-templated mesopores and micropores are formed. Adding Fe_3O_4 nanoparticles as catalysts poses no additional steps during the fabrication procedure, and the catalyst particles are well-distributed over the final Fe@ChiSuc carbon due to surface diffusion of particles during carbonization at 1000 °C. Textural analysis based on N_2-physisorption revealed that $ChiSuc_{no–silica}$, ChiSuc, and Fe@ChiSuc are microporous, micro-/mesoporous, and mesoporous carbons with 612 ± 40 $m^2\,g^{-1}$, 553 ± 46 $m^2\,g^{-1}$, and 343 ± 35 $m^2\,g^{-1}$ BET specific surface area, respectively. Additionally, the capability of ChiSuc for electro-generation of H_2O_2 was demonstrated, and the impact of open ice-templated pore network on the measured H_2O_2 concentrations and achieved current efficiency (CE) was discussed. Accordingly, the CE for H_2O_2 production by $ChiSuc_{no–silica}$ was half of that by ChiSuc (26 ± 2 %), being attributed to the collapsed structure of $ChiSuc_{no–silica}$ given its highest shrinkage due to the lack of binding agents (colloidal silica).

The catalytic activity of Fe@ChiSuc at neutral pH was illustrated using CBZ as a persistent model pollutant, revealing the negligible contribution of anodic oxidation, H_2O_2 oxidation, and (electro-)adsorption at a cathodic potential of -0.17 V. Moreover, Fe@ChiSuc removed CBZ and SMX at both pH 3 and pH 7 with negligible Fe leaching, showing the dominant HEF reaction.

Successive runs illustrated the crucial role of (i) the transport mechanisms, e.g., surface diffusion and pore diffusion, inside the ice-templated pore network of the carbon; (ii) the pollutant's charge and its repulsive or attractive interaction with the electrodes' surface; and (iii) the capillary forces caused by ice-templated pores for an effective HEF process. Furthermore, reusability of the electrode over consecutive runs was demonstrated, pointing out the importance of the post-treatment type after each run on the recorded efficiency. These results unveil the tremendous potential of the proposed synthesis method for fabricating binder-free freestanding catalyst-containing carbons with hierarchical porosity for different applications, particularly as a potentially scalable and efficient electrode for water and wastewater treatment via HEF processes.

Acknowledgement

M.M. appreciates the funding from the European Union's Horizon 2020 research and innovation program under the Marie Skłodowska-Curie grant agreement No 676070. This communication reflects only the authors' view, and the Research Executive Agency of the EU is not responsible for any use that may be made of the information it contains. M.W. acknowledges DFG funding through the Gottfried Wilhelm Leibniz Award 2019 (WE 4678/12-1). This work was conducted in part at the Competence Center for Industrial Electrochemistry ELECTRA, which is supported by the "European Regional Development Fund (ERDF) and the Federal State of North Rhine-Westphalia (grant no. ERDF 05 00 07 7)

References

[1] Enric Brillas, Ignasi Sirés, and Mehmet A Oturan. Electro-fenton process and related electrochemical technologies based on fenton's reaction chemistry. *Chemical reviews*, 109(12):6570–6631, 2009.

[2] PV Nidheesh and R Gandhimathi. Trends in electro-fenton process for water and wastewater treatment: an overview. *Desalination*, 299:1–15, 2012.

[3] Brian P Chaplin. Critical review of electrochemical advanced oxidation processes for water treatment applications. *Environmental Science: Processes & Impacts*, 16(6):1182–1203, 2014.

[4] Minghua Zhou, Mehmet A Oturan, and Ignasi Sires. *Electro-Fenton Process*. Springer, 2018.

[5] Ignasi Sirés, Enric Brillas, Mehmet A Oturan, Manuel A Rodrigo, and Marco Panizza. Electrochemical advanced oxidation processes: today and tomorrow. a review. *Environmental Science and Pollution Research*, 21(14):8336–8367, 2014.

[6] Soliu O Ganiyu, Minghua Zhou, and Carlos A Martínez-Huitle. Heterogeneous electro-fenton and photoelectro-fenton processes: a critical review of fundamental principles and application for water/wastewater treatment. *Applied Catalysis B: Environmental*, 235:103–129, 2018.

[7] PV Nidheesh. Heterogeneous fenton catalysts for the abatement of organic pollutants from aqueous solution: a review. *Rsc Advances*, 5(51):40552–40577, 2015.

[8] Konstantinos V Plakas, Anastasios J Karabelas, Stella D Sklari, and Vassilis T Zaspalis. Toward the development of a novel electro-fenton system for eliminating toxic organic substances from water. part 1. in situ generation of hydrogen peroxide. *Industrial & Engineering Chemistry Research*, 52(39):13948–13956, 2013.

[9] Mojtaba Mohseni, Kristof Demeestere, Gijs Du Laing, Süleyman Yüce, Robert G Keller, and Matthias Wessling. Cnt microtubes with entrapped fe3o4 nanoparticles remove micropollutants through a heterogeneous electro-fenton process at neutral ph. *Advanced Sustainable Systems*, page 2100001, 2021.

[10] Thi May Do, Ji Young Byun, and Sang Hoon Kim. An electro-fenton system using magnetite coated metallic foams as cathode for dye degradation. *Catalysis Today*, 295:48–55, 2017.

[11] Wei Zhou, Ljiljana Rajic, Long Chen, Kaikai Kou, Yani Ding, Xiaoxiao Meng, Yan Wang, Biruk Mulaw, Jihui Gao, Yukun Qin, et al. Activated carbon as effective cathode material in iron-free electro-fenton process: Integrated h2o2 electrogeneration, activation, and pollutants adsorption. *Electrochimica acta*, 296:317–326, 2019.

[12] Yan Zhang, Mingming Gao, Shu-Guang Wang, Weizhi Zhou, Yuanhua Sang, and Xin-Hua Wang. Integrated electro-fenton process enabled by a rotating fe3o4/gas diffusion cathode for simultaneous generation and activation of h2o2. *Electrochimica Acta*, 231:694–704, 2017.

[13] Chao Zhang, Minghua Zhou, Gengbo Ren, Xinmin Yu, Liang Ma, Jie

Yang, and Fangke Yu. Heterogeneous electro-fenton using modified iron–carbon as catalyst for 2, 4-dichlorophenol degradation: influence factors, mechanism and degradation pathway. *Water research*, 70:414–424, 2015.

[14] Soliu O Ganiyu, Thi Xuan Huong Le, Mikhael Bechelany, Giovanni Esposito, Eric D van Hullebusch, Mehmet A Oturan, and Marc Cretin. A hierarchical cofe-layered double hydroxide modified carbon-felt cathode for heterogeneous electro-fenton process. *Journal of Materials Chemistry A*, 5(7):3655–3666, 2017.

[15] Yujing Wang, Guohua Zhao, Shouning Chai, Hongying Zhao, and Yanbin Wang. Three-dimensional homogeneous ferrite-carbon aerogel: one pot fabrication and enhanced electro-fenton reactivity. *ACS applied materials & interfaces*, 5(3):842–852, 2013.

[16] Wei Chen, Xiaoling Yang, Jianfei Huang, Yihua Zhu, Yin Zhou, Yifan Yao, and Chunzhong Li. Iron oxide containing graphene/carbon nanotube based carbon aerogel as an efficient e-fenton cathode for the degradation of methyl blue. *Electrochimica Acta*, 200:75–83, 2016.

[17] Kai Liu, Joseph Che-Chin Yu, Heng Dong, Jeffrey CS Wu, and Michael R Hoffmann. Degradation and mineralization of carbamazepine using an electro-fenton reaction catalyzed by magnetite nanoparticles fixed on an electrocatalytic carbon fiber textile cathode. *Environmental science & technology*, 52(21):12667–12674, 2018.

[18] Hongying Zhao, Lin Qian, Xiaohong Guan, Deli Wu, and Guohua Zhao. Continuous bulk fecuc aerogel with ultradispersed metal nanoparticles:

an efficient 3d heterogeneous electro-fenton cathode over a wide range of ph 3–9. *Environmental science & technology*, 50(10):5225–5233, 2016.

[19] Jinpo Li, Zhihui Ai, and Lizhi Zhang. Design of a neutral electro-fenton system with fe@ fe2o3/acf composite cathode for wastewater treatment. *Journal of hazardous materials*, 164(1):18–25, 2009.

[20] Orlando García-Rodríguez, Jennifer A Bañuelos, Abdellatif El-Ghenymy, Luis A Godínez, Enric Brillas, and Francisco J Rodríguez-Valadez. Use of a carbon felt–iron oxide air-diffusion cathode for the mineralization of malachite green dye by heterogeneous electro-fenton and uva photoelectro-fenton processes. *Journal of Electroanalytical Chemistry*, 767:40–48, 2016.

[21] Li Zhuang, Shungui Zhou, Yongtao Li, Tinglin Liu, and Deyin Huang. In situ fenton-enhanced cathodic reaction for sustainable increased electricity generation in microbial fuel cells. *Journal of Power Sources*, 195(5):1379–1382, 2010.

[22] Min Sun, Xiao-Rui Ru, and Lin-Feng Zhai. In-situ fabrication of supported iron oxides from synthetic acid mine drainage: high catalytic activities and good stabilities towards electro-fenton reaction. *Applied Catalysis B: Environmental*, 165:103–110, 2015.

[23] Liang Liang, Fangke Yu, Yiran An, Mengmeng Liu, and Minghua Zhou. Preparation of transition metal composite graphite felt cathode for efficient heterogeneous electro-fenton process. *Environmental Science and Pollution Research*, 24(2):1122–1132, 2017.

[24] Zhangweihao Pan, Kun Wang, Yi Wang, Panagiotis Tsiakaras, and Shuqin Song. In-situ electrosynthesis of hydrogen peroxide and wastewater treatment application: a novel strategy for graphite felt activation. *Applied Catalysis B: Environmental*, 237:392–400, 2018.

[25] Thi Xuan Huong Le, Mikhael Bechelany, and Marc Cretin. Carbon felt based-electrodes for energy and environmental applications: A review. *Carbon*, 122:564–591, 2017.

[26] Yi Wang, Yuhui Liu, Kun Wang, Shuqin Song, Panagiotis Tsiakaras, and Hong Liu. Preparation and characterization of a novel koh activated graphite felt cathode for the electro-fenton process. *Applied Catalysis B: Environmental*, 165:360–368, 2015.

[27] Weilu Yang, Minghua Zhou, Jingju Cai, Liang Liang, Gengbo Ren, and Lili Jiang. Ultrahigh yield of hydrogen peroxide on graphite felt cathode modified with electrochemically exfoliated graphene. *Journal of Materials Chemistry A*, 5(17):8070–8080, 2017.

[28] Wenyue Li, Jianguo Liu, and Chuanwei Yan. The electrochemical catalytic activity of single-walled carbon nanotubes towards vo2+/vo2+ and v3+/v2+ redox pairs for an all vanadium redox flow battery. *Electrochimica Acta*, 79:102–108, 2012.

[29] Xiaolan Zhou, Dong Xu, Yuancai Chen, and Yongyou Hu. Enhanced degradation of triclosan in heterogeneous e-fenton process with mof-derived hierarchical mn/fe@ pc modified cathode. *Chemical Engineering Journal*, 384:123324, 2020.

[30] Peike Cao, Xie Quan, Kun Zhao, Shuo Chen, Hongtao Yu, and Junfeng Niu. Selective electrochemical h2o2 generation and activation on a bifunctional catalyst for heterogeneous electro-fenton catalysis. *Journal of hazardous materials*, 382:121102, 2020.

[31] Ian Ross, Jeffrey McDonough, Jonathan Miles, Peter Storch, Parvathy Thelakkat Kochunarayanan, Erica Kalve, Jake Hurst, Soumitri S. Dasgupta, and Jeff Burdick. A review of emerging technologies for remediation of pfass. *Remediation Journal*, 28(2):101–126, 2018.

[32] Katarzyna H Kucharzyk, Ramona Darlington, Mark Benotti, Rula Deeb, and Elisabeth Hawley. Novel treatment technologies for pfas compounds: A critical review. *Journal of environmental management*, 204:757–764, 2017.

[33] Jaclyn E Cañas, Monique Long, Shawna Nations, Rodica Vadan, Lenore Dai, Mingxiang Luo, Ramya Ambikapathi, E Henry Lee, and David Olszyk. Effects of functionalized and nonfunctionalized single-walled carbon nanotubes on root elongation of select crop species. *Environmental Toxicology and Chemistry: An International Journal*, 27(9):1922–1931, 2008.

[34] Karin Aschberger, Helinor J Johnston, Vicki Stone, Robert J Aitken, Steven M Hankin, Sheona AK Peters, C Lang Tran, and Frans M Christensen. Review of carbon nanotubes toxicity and exposure—appraisal of human health risk assessment based on open literature. *Critical reviews in toxicology*, 40(9):759–790, 2010.

[35] Minfang Zhang, Yinmei Deng, Mei Yang, Hideaki Nakajima, Masako Yudasaka, Sumio Iijima, and Toshiya Okazaki. A simple method for removal of carbon nanotubes from wastewater using hypochlorite. *Scientific reports*, 9(1):1–7, 2019.

[36] Mojtaba Mohseni, Nikolai Utsch, Christian Marcks, Kristof Demeestere, Gijs Du Laing, Süleyman Yüce, Robert G Keller, and Matthias Wessling. Freestanding nitrogen-doped carbons with hierarchical porosity for environmental applications: A green templating route with bio-based precursors. *Global Challenges*, page 2100062, 2021.

[37] Matthias Thommes, Katsumi Kaneko, Alexander V Neimark, James P Olivier, Francisco Rodriguez-Reinoso, Jean Rouquerol, and Kenneth SW Sing. Physisorption of gases, with special reference to the evaluation of surface area and pore size distribution (iupac technical report). *Pure and Applied Chemistry*, 87(9-10):1051–1069, 2015.

[38] Jan-Bernd Vennekötter, Thomas Scheuermann, Robert Sengpiel, and Matthias Wessling. The electrolyte matters: Stable systems for high rate electrochemical co2 reduction. *Journal of CO2 Utilization*, 32:202–213, 2019.

[39] Raquel F Pupo Nogueira, Mirela C Oliveira, and Willian C Paterlini. Simple and fast spectrophotometric determination of h2o2 in photo-fenton reactions using metavanadate. *Talanta*, 66(1):86–91, 2005.

[40] Regina CC Costa, Flavia CC Moura, JD Ardisson, JD Fabris, and RM Lago. Highly active heterogeneous fenton-like systems based on

fe0/fe3o4 composites prepared by controlled reduction of iron oxides. *Applied Catalysis B: Environmental*, 83(1-2):131–139, 2008.

[41] Jumeng Zheng, David Salamon, Leon Lefferts, Matthias Wessling, and Louis Winnubst. Ceramic microfluidic monoliths by ice templating. *Microporous and mesoporous materials*, 134(1-3):216–219, 2010.

[42] Stephanie-Angelika Wohlgemuth, Filipe Vilela, Maria-Magdalena Titirici, and Markus Antonietti. A one-pot hydrothermal synthesis of tunable dual heteroatom-doped carbon microspheres. *Green chemistry*, 14(3):741–749, 2012.

[43] Robin J White, Noriko Yoshizawa, Markus Antonietti, and Maria-Magdalena Titirici. A sustainable synthesis of nitrogen-doped carbon aerogels. *Green chemistry*, 13(9):2428–2434, 2011.

[44] Tim-Patrick Fellinger, Frédéric Hasché, Peter Strasser, and Markus Antonietti. Mesoporous nitrogen-doped carbon for the electrocatalytic synthesis of hydrogen peroxide. *Journal of the American Chemical Society*, 134(9):4072–4075, 2012.

[45] Frédéric Hasché, Mehtap Oezaslan, Peter Strasser, and Tim-Patrick Fellinger. Electrocatalytic hydrogen peroxide formation on mesoporous non-metal nitrogen-doped carbon catalyst. *Journal of Energy Chemistry*, 25(2):251–257, 2016.

[46] Hai-Wei Liang, Xiaodong Zhuang, Sebastian Brüller, Xinliang Feng, and Klaus Müllen. Hierarchically porous carbons with optimized nitrogen

doping as highly active electrocatalysts for oxygen reduction. *Nature communications*, 5(1):1–7, 2014.

[47] Marta Nunes, Inês M Rocha, Diana M Fernandes, Ana S Mestre, Cosme N Moura, Ana P Carvalho, Manuel FR Pereira, and Cristina Freire. Sucrose-derived activated carbons: electron transfer properties and application as oxygen reduction electrocatalysts. *RSC advances*, 5(124):102919–102931, 2015.

[48] Alireza Khataee, Saeed Sajjadi, Shima Rahim Pouran, Aliyeh Hasanzadeh, and Sang Woo Joo. A comparative study on electrogeneration of hydrogen peroxide through oxygen reduction over various plasma-treated graphite electrodes. *Electrochimica Acta*, 244:38–46, 2017.

[49] Fangke Yu, Minghua Zhou, Lei Zhou, and Rudan Peng. A novel electro-fenton process with h2o2 generation in a rotating disk reactor for organic pollutant degradation. *Environmental Science & Technology Letters*, 1(7):320–324, 2014.

[50] Xinmin Yu, Minghua Zhou, Youshuang Hu, K Groenen Serrano, and Fangke Yu. Recent updates on electrochemical degradation of bio-refractory organic pollutants using bdd anode: a mini review. *Environmental Science and Pollution Research*, 21(14):8417–8431, 2014.

[51] Ali Özcan, Yücel Şahin, A Savaş Koparal, and Mehmet A Oturan. Carbon sponge as a new cathode material for the electro-fenton process: comparison with carbon felt cathode and application to degradation of

synthetic dye basic blue 3 in aqueous medium. *Journal of Electroanalytical Chemistry*, 616(1-2):71–78, 2008.

[52] Wei Zhou, Jihui Gao, Yani Ding, Haiqian Zhao, Xiaoxiao Meng, Yan Wang, Kaikai Kou, Yiqun Xu, Shaohua Wu, and Yukun Qin. Drastic enhancement of h2o2 electro-generation by pulsed current for ibuprofen degradation: Strategy based on decoupling study on h2o2 decomposition pathways. *Chemical Engineering Journal*, 338:709–718, 2018.

[53] Yujing Wang, Hongying Zhao, Shouning Chai, Yabo Wang, Guohua Zhao, and Dongming Li. Electrosorption enhanced electro-fenton process for efficient mineralization of imidacloprid based on mixed-valence iron oxide composite cathode at neutral ph. *Chemical engineering journal*, 223:524–535, 2013.

[54] Yingshi Zhu, Shan Qiu, Fang Ma, Guojun Li, Fengxia Deng, and Yanshi Zheng. Melamine-derived carbon electrode for efficient h2o2 electrogeneration. *Electrochimica Acta*, 261:375–383, 2018.

[55] Laura Piai, Jouke E Dykstra, Mahesa G Adishakti, Marco Blokland, Alette AM Langenhoff, and Albert van der Wal. Diffusion of hydrophilic organic micropollutants in granular activated carbon with different pore sizes. *Water research*, 162:518–527, 2019.

[56] AI Moral-Rodríguez, R Leyva-Ramos, R Ocampo-Pérez, J Mendoza-Barron, IN Serratos-Alvarez, and JJ Salazar-Rabago. Removal of ronidazole and sulfamethoxazole from water solutions by adsorption on gran-

ular activated carbon: equilibrium and intraparticle diffusion mechanisms. *Adsorption*, 22(1):89–103, 2016.

[57] Yang Huang, Jinsong Guo, Peng Yan, Hao Gong, and Fang Fang. Sorption-desorption behavior of sulfamethoxazole, carbamazepine, bisphenol a and 17α-ethinylestradiol in sewage sludge. *Journal of hazardous materials*, 368:739–745, 2019.

[58] Jurate Virkutyte and Rajender Varma. *Treatment of micropollutants in water and wastewater*. IWA Publishing, 2010.

[59] Guosheng Shi, Yue Shen, Jian Liu, Chunlei Wang, Ying Wang, Bo Song, Jun Hu, and Haiping Fang. Molecular-scale hydrophilicity induced by solute: molecular-thick charged pancakes of aqueous salt solution on hydrophobic carbon-based surfaces. *Scientific reports*, 4(1):1–5, 2014.

[60] Fatemeh Keramatnia, Ali Shayanfar, and Abolghasem Jouyban. Thermodynamic solubility profile of carbamazepine–cinnamic acid cocrystal at different ph. *Journal of pharmaceutical sciences*, 104(8):2559–2565, 2015.

[61] Rutwij A Dave and Marilyn E Morris. A quantitative threshold for high/low extent of urinary excretion of compounds in humans. *Biopharmaceutics & drug disposition*, 37(5):287–309, 2016.

[62] Sheng-Peng Sun, Xia Zeng, and Ann T Lemley. Kinetics and mechanism of carbamazepine degradation by a modified fenton-like reaction with ferric-nitrilotriacetate complexes. *Journal of hazardous materials*, 252:155–165, 2013.

[63] Ana I Zárate-Guzmán, Linda V González-Gutiérrez, Luis A Godínez, Alejandro Medel-Reyes, Francisco Carrasco-Marín, and Luis A Romero-Cano. Towards understanding of heterogeneous fenton reaction using carbon-fe catalysts coupled to in-situ h2o2 electro-generation as clean technology for wastewater treatment. *Chemosphere*, 224:698–706, 2019.

[64] Nicola C Rudd, Susan Cannan, Eleni Bitziou, Ilenia Ciani, Anna L Whitworth, and Patrick R Unwin. Fluorescence confocal laser scanning microscopy as a probe of ph gradients in electrode reactions and surface activity. *Analytical chemistry*, 77(19):6205–6217, 2005.

[65] Lilja Nielsen, Mark J Biggs, William Skinner, and Teresa J Bandosz. The effects of activated carbon surface features on the reactive adsorption of carbamazepine and sulfamethoxazole. *Carbon*, 80:419–432, 2014.

[66] Heng Zhao, Xue Liu, Zhen Cao, Yi Zhan, Xiaodong Shi, Yi Yang, Junliang Zhou, and Jiang Xu. Adsorption behavior and mechanism of chloramphenicols, sulfonamides, and non-antibiotic pharmaceuticals on multi-walled carbon nanotubes. *Journal of hazardous materials*, 310:235–245, 2016.

[67] Mojtaba Mohseni, Pietro Postacchini, Kristof Demeestere, Gijs Du Laing, Süleyman Yüce, and Matthias Wessling. Freestanding pac/cnt microtubes remove sulfamethoxazole from water through a temperature-assisted cyclic process. *Journal of hazardous materials*, 392, 2020.

[68] Josué Daniel García-Espinoza and Petia Mijaylova Nacheva. Effect

of electrolytes on the simultaneous electrochemical oxidation of sulfamethoxazole, propranolol and carbamazepine: behaviors, by-products and acute toxicity. *Environmental Science and Pollution Research*, 26(7):6855–6867, 2019.